Supporting Information

MOF-Derived Ultrathin Carbon Nanosheets Integrated with Telluride Nanoparticles: Synergistic Polysulfide Adsorption and Catalytic Sites for Enhanced Sulfur Redox Reactions

Wei Bi,[a,+] Canhuang Li,[b,+] Dawei Yang,[a,] Yu-Zhen Zhang,[c] Lei Hu,[c] Qianhong Gong,[a] Jie Zhang,[a] Yongcai Zhang,[d] Mengyao Li,[e] Jishi Wei,[f] Yingtang Zhou,[g,*] Dan Zhou,[a] Tianli Wu,[a] Li-Feng Chen,[c,h,*] Andreu Cabot[b,*]*

[a] Henan Key Laboratory of Quantum Materials and Quantum Energy, School of Quantum Information Future Technology, Henan University, Kaifeng, 475004, China.
[b] Catalonia Institute for Energy Research - IREC, Sant Adrià de Besòs, Barcelona, 08930, Spain.
[c] Division of Nanomaterials & Chemistry, Hefei National Research Center for Physical Sciences at the Microscale, National Key Laboratory of Precision and Intelligent Chemistry, School of Chemistry and Materials Science, CAS Key Laboratory of Mechanical Behavior and Design of Materials (LMBD), University of Science and Technology of China, Hefei, Anhui 230026, PR China.
[d] School of Chemistry and Chemical Engineering, Yangzhou University, Yangzhou 225009, China.
[e] Key Laboratory of Materials Physics of Ministry of Education, School of Physics and Microelectronics, Zhengzhou University, Daxue Road 75, Zhengzhou, 450052 China.
[f] Longzihu New Energy Laboratory, Zhengzhou Institute of Emerging Industrial Technology, College of Chemistry and Molecular Sciences, Henan University, Kaifeng, Henan 475004, PR China.
[g] Zhejiang Key Laboratory of Petrochemical Environmental Pollution Control, National Engineering Research Center for Marine Aquaculture, Zhejiang Ocean University, Zhoushan, Zhejiang, 316004 China.
[h] Lead contact
[+] These authors contributed equally to this work.
* Corresponding authors: Dr. D. W. Yang (dwyang@henu.edu.cn), Prof. L. F. Chen (chenlf@ustc.edu.cn), Prof. Y. T. Zhou (zhouyingtang@zjou.edu.cn), and Prof. A. Cabot (acabot@irec.cat).

Experimental Section

Synthesis of Zeolitic Imidazolate Framework (ZIF-8): A 5.56 g (0.067 mol) amount of 2-methylimidazole (99%, Acros Organics) was dissolved in 70 mL of deionized water. The obtained solution was poured into 30 mL of a deionized water solution containing 0.3 g (0.00137 mol) of $Zn(CH_3COO)_2 \cdot 2H_2O$ (98%, Alfa Aesar), and the mixed solution was stirred for 24 h at room temperature. The obtained white precipitate was collected, washed with deionized water several times, and dried overnight.

Synthesis of $FeTe_2$/CN: A 1000 mg amount of the as-obtained ZIF-8 powder and 1000 mg of $Fe(C_5H_7O_2)_3$ powder (99%, Sigma-Aldrich). Grind and mix the resulting powder and tellurium powder (99%, Sigma-Aldrich) were placed in two separated porcelain boats. The porcelain boats were placed within a tubular furnace having an Ar flow (100 mL min^{-1}), with the Fe@ZIF-8 boat upstream and the tellurium powder downstream. The furnace was heated to 620 °C at a heating rate of 10 °C min^{-1} and maintained at this temperature for 8 h. After cooling to room temperature, the $FeTe_2$/CN powder was collected.

Synthesis of CN: CN was obtained by annealing ZIF-8 powder and tellurium powder in the same conditions but without $Fe(C_5H_7O_2)_3$ powder. The obtained black powder was immersed in a 2 M HCl solution and stirred for 24 h to remove Zn. The precipitate was collected by filtration, washed with ethanol, and dried at 60 °C overnight.

Synthesis of S@$FeTe_2$/CN, S@CN, and S@Super P: Sulfur was incorporated by means of a simple melting diffusion process. To obtain S@$FeTe_2$/CN, as-prepared $FeTe_2$/CN and sublimed sulfur (99.98%, Sigma-Aldrich) were well mixed at a 1:3 weight ratio and heated at 155 °C for 12 h in a glass bottle under in vacuum. To remove the redundant sulfur outside of $FeTe_2$/CN, the powder was immersed in a 10 mL CS_2 and ethanol solution (1:4, volume ratio) for 10 min twice. For comparison, S@CN and S@Super P (Super P from Alfa Aesar, 99%) were obtained by the same process.

Materials Characterization: Chemical compositions were analyzed by X-ray diffraction (XRD) patterns recorded at room temperature using a Bruker AXS D8 Advance X-ray diffractometer with Cu K radiation (λ = 1.5106 Å) operating at 40 kV and 40 mA. Field emission scanning electron microscopy (FESEM) analyses were carried on a ZEISS Auriga microscope with an energy dispersive X-ray spectroscopy (EDS) detector operating at 20 kV.

Transmission electron microscopy (TEM) characterization was carried out on a Zeiss Libra 120 (Carl Zeiss, Jena, Germany) operating at 120 kV. High-resolution TEM (HRTEM) and scanning TEM (STEM) studies were carried out using a field emission gun FEI Tecnai F20 microscope at 200 kV with a tested lattice resolution of 0.1 nm. High angle annular dark-field (HAADF) STEM was combined with electron energy loss spectroscopy in the Tecnai microscope by using a Gatan Quantum filter. X-ray photoelectron spectroscopy (XPS) measurements were conducted at 150 W using a Phoibos 150 MCD-9 detector. Thermogravimetric measurements (TGA) were performed to record the ratio of S within prepared composites. UV−vis absorption spectra were tested on a PerkinElmer Lambda 950 UV−vis spectrophotometer. Nitrogen adsorption−desorption isotherms were measured to evaluate the specific surface area and the pore size distribution using a Brunauer−Emmett−Teller method (Tristar II 3020 Micromeritics system).

Electrochemical Measurements: Working electrodes were prepared by mixing the active materials (S@$FeTe_2$/CN, S@CN, and S@Super P), Super P, and PVDF binders with a weight ratio of 8:1:1 in N-methyl-2-pyrrolidone (NMP, 99.5%, Acros Organics). Then the slurry was coated on an aluminum foil and dried at 60 °C under vacuum overnight. Subsequently, the coated aluminum foil was punched into small disks having a sulfur loading of about 1.1 mg cm^{-2} and were assembled into coin cells in an Ar-filled glovebox. Li foil was used as the counter electrode and Celgard 2400 membranes as separators. The electrolyte was prepared by dissolving 1.0 M lithium bis(trifluoromethanesulfonyl)imide (LiTFSI) (99%, Acros Organics) in a mixture of DOL (99.5%, Alfa Aesar) and DME (99%, Honeywell) (1:1 v/v) with the addition of 0.2 M $LiNO_3$ (99.98%, Alfa Aesar). The amount of electrolyte was about 20 μL for each coin cell. In the higher sulfur loading electrodes of 3.3 mg cm^{-2}, 50 μL of electrolyte was added in these coin cells. Before cycling, all coin cells were aged for several hours to ensure a sufficient penetration of the electrolyte into the electrode. Galvanostatic charge/discharge (GCD) measurements were performed with a voltage window of 1.7−2.8 V vs Li^+/Li at different current densities using a Neware BTS4008 battery cycler. Cyclic voltammetry (CV) tests were performed on a BCS-810 battery tester from Bio Logic at different scan rates in the range of 0.1−0.4 mV s^{-1}. Electrochemical impedance spectroscopy (EIS) tests were carried out using a sinusoidal voltage with amplitude of 10 mV in the frequency range 100 kHz to 0.01 Hz.

Synthesis of Li_2S_4 Solution and Adsorption Test: Sulfur and Li_2S (99.9%, Alfa Aesar) with a molar ratio of 3:1 were added to appropriate amounts of DME and DOL (volume ratio of 1:1) under vigorous magnetic stirring overnight, until a dark brown solution was formed. For the polysulfide absorption ability test, 20 mg of active materials ($FeTe_2$/CN, CN, and Super P) was immersed into 3.0 mL of 10×10^{-3} M Li_2S_4 solution, which was shaken and aged overnight.

Symmetric Cell Assembly and Measurements: The $FeTe_2$/CN (CN and Super P) composite was mixed with Super P and PVDF binder with a weight ratio of 8:1:1 in NMP. Then the slurry was coated onto the Al foil and dried at 60 °C for 12 h in a vacuum oven. Two pieces of the same electrode (average loading about 0.5 mg cm^{-2}) were used as identical working and counter electrodes. A 40 μL amount of electrolyte containing 0.5 M Li_2S_6 and 1 M LiTFSI dissolved in DOL/DME (v/v = 1:1) was added into each coin cell.

Measurement of Nucleation of Li_2S

Nucleation of Li_2S was conducted in CR2032 coin cells. 1 mg host materials ($FeTe_2$/CN, CN and Super P) were loaded on the carbon papers applied as working electrodes. Li foil worked as the counter electrode. The catholyte consisted of 20 μL of 0.25 M Li_2S_8 and 1.0 M LiTFSI in tetraethylene glycol dimethyl ether solution. Another 20 μL amount of 1 M LiTFSI solution without Li_2S_8 was used as anolyte. The cells were first discharged at a current of 0.112 mA to 2.19 V and then hold the voltage at 2.05 V until the current decreased to 10^{-2} mA for Li_2S nucleation and growth.

Details of Theoretical calculations

The first principle calculations were performed by the Vienna ab initio simulation package (VASP) on MedeA platform using the generalized gradient approximation (GGA) and Perdew-Burke-Ernzerhof (PBE) method base on density functional theory (DFT).[1] The projector augmented wave (PAW) was used to describe ions and electron interaction. The kinetic energy cutoff was set at 520 eV.

NC and $FeTe_2$ were employed as the models for further determine the intrinsic mechanism for the excellent Li-S battery activity. The cell parameters of NC and $FeTe_2$ are a = b = 9.84000 Å, c = 16.80000 Å and a = b = 8.86900 Å, c = 21.27130 Å, respectively. In the vertical direction, a vacuum layer of about 15 Å in thickness was introduced to avoid the interaction between neighboring image structures.

In all the calculations, we use 3 × 3 × 1 for the Monkhorst-Pack k-point for periodic crystal structure and surface model. The convergence threshold for energy was set at 10−5 eV.[2] The equilibrium lattice constants were optimized with maximum stress on each atom within 0.05 eV/Å. In addition, transition states of Na ion diffusion were calculated by the climbing-imagenudged elastic band (CI-NEB) method.[3]

The adsorption energy (ΔE_{ads}) were defined as follows:[4]

$E_{ads} = E_{ad/sub} - E_{ad} - E_{sub}$

where $E_{ad/sub}$, E_{ad} and E_{sub} are the optimized adsorbate/substrate system, the adsorbate in the structure and the clean substrate respectively. Usually, a more negative E_{ads} value reflects a stronger adsorption.

The free energy was calculated using the equation:

$\Delta G = \Delta E + \Delta ZPE - \Delta TS$

Where ΔG, ΔE, ΔZPE, and TS represented the free energy, total energy from DFT calculations, zero-point energy, and entropic contributions (T was set to be 300 K), respectively.

Fig. S1 $FeTe_2$/CN was generated in situ on a larger scale using high-purity tellurium powder.

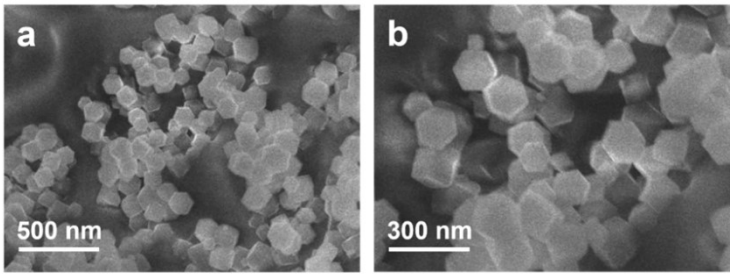

Fig. S2 a,b) FESEM images of ZIF-8 with different magnifications.

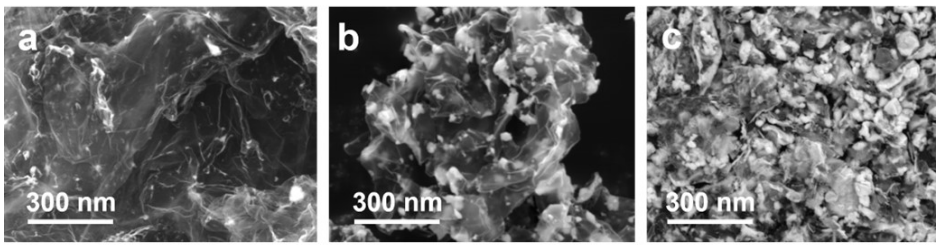

Fig. S3 SEM images of the $FeTe_2$/CN with the ZIF-8 and $Fe(C_5H_7O_2)_3$ mass ratio of a) 1:1, b) 1:2, and c) 1:3.

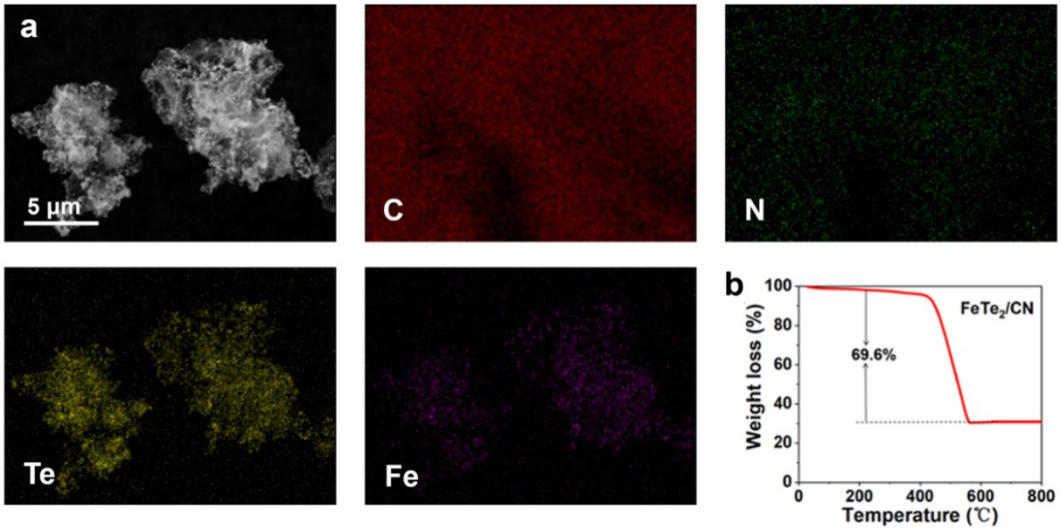

Fig. S4 a) SEM images of the $FeTe_2$/CN and corresponding EDX elemental mapping of Te, N, C, Fe. b) TGA curves of the samples.

The TGA curves were characterized under the air atmosphere with the temperature ranging from 25 to 800 °C at a heating rate of 10 °C min^{-1}. It can be observed that when the temperature range was between 25 and 200 °C, the samples have initial marginal weight loss, which is due to the evaporation of free water and physically adsorbed water in the material during the temperature rise, resulting in the quality reduction. Besides, the severe mass loss of materials from 300 °C to 600 °C can be attributed to the reaction of N-doped carbonaceous components with oxygen, the generation of carbon dioxide gas. As shown in Figure S4b, according to the TGA result and oxidation product ($Fe_2Te_3O_8$), the carbon content of $FeTe_2$/CN was calculated to be 69.6%.

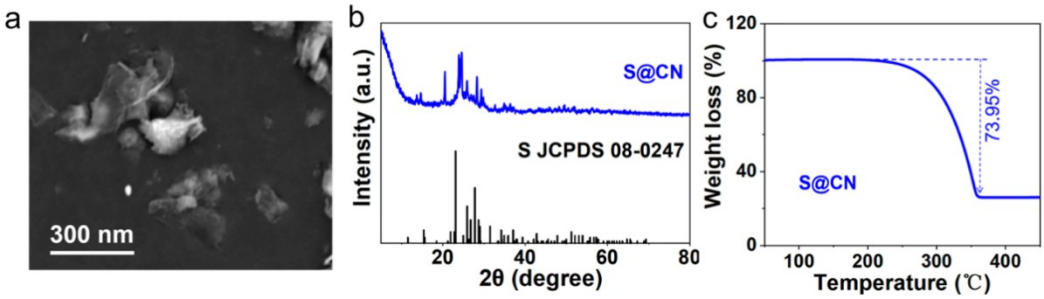

Fig. S5 a) SEM image of CN. b) XRD pattern of S@CN. c) TGA curve measured in N_2 of S@CN.

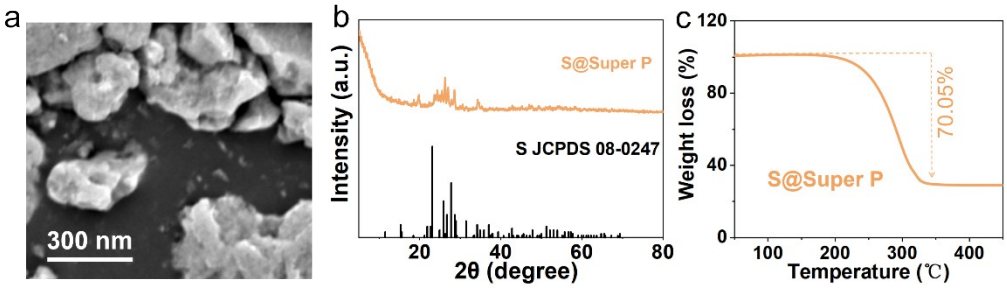

Fig. S6 a) SEM image of Super P. b) XRD pattern of S@Super P. c) TGA curve measured in N_2 of S@Super P.

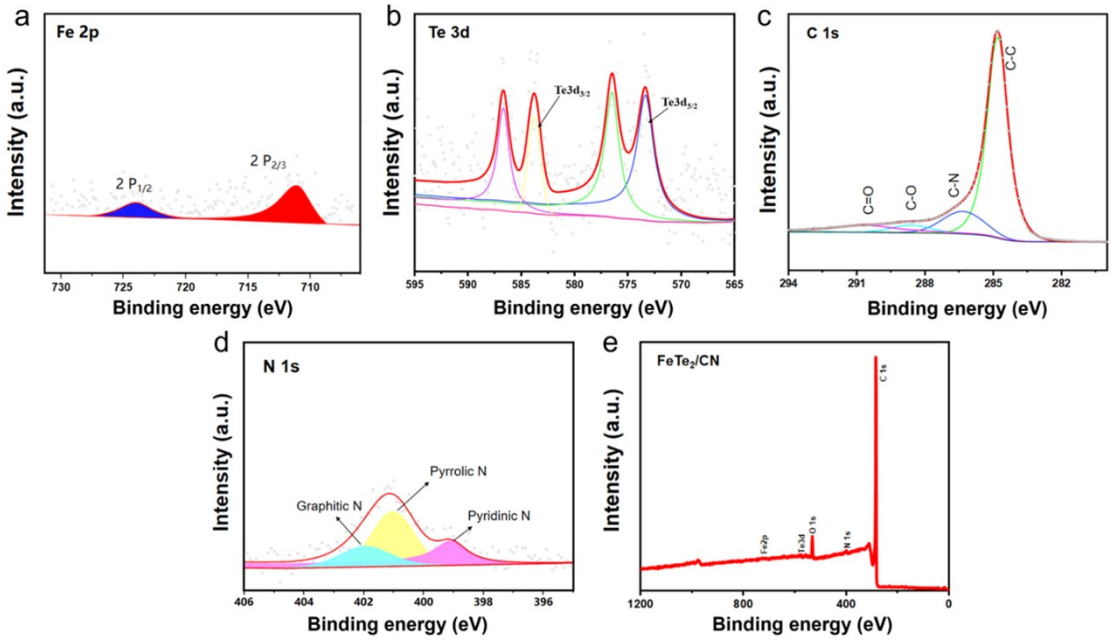

Fig. S7 High resolution XPS spectra of the regions: a) Fe 2p, b) Te 3d, c) C 1s, and d) N 1s. e) Survey XPS spectrum.

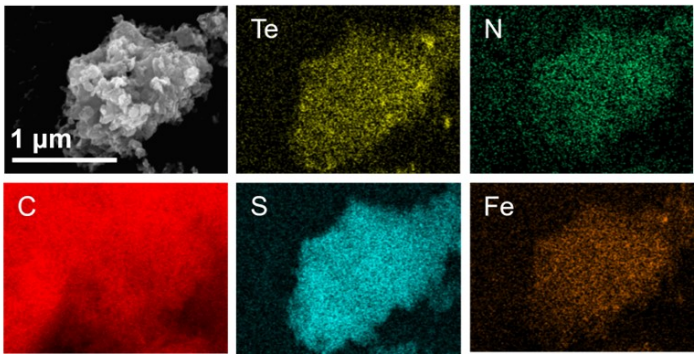

Fig. S8 SEM images of the S@$FeTe_2$/CN and corresponding EDX elemental mapping of Te, N, C, S, Fe.

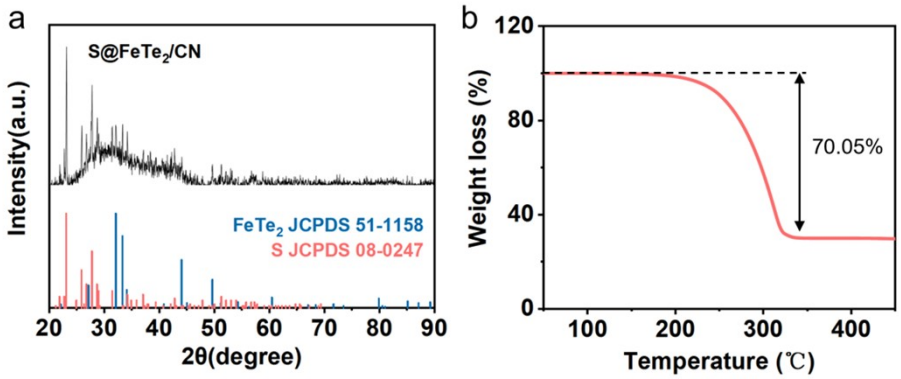

Fig. S9 a) XRD pattern of S@$FeTe_2$/CN, including reference patterns for cubic $FeTe_2$ (JCPDS No. 51-1158) and cubic sulfur (JCPDS No. 08-0247). b) TGA curve of S@$FeTe_2$/CN composite.

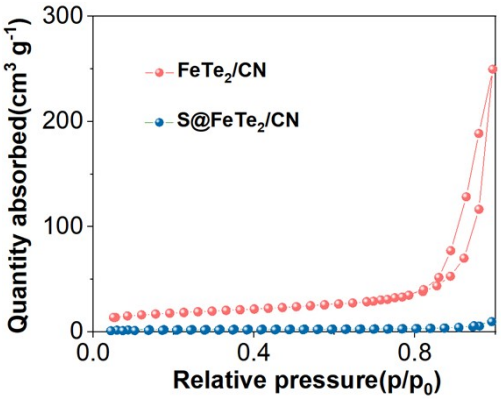

Fig. S10 N_2 adsorption-desorption isotherms of S@$FeTe_2$/CN.

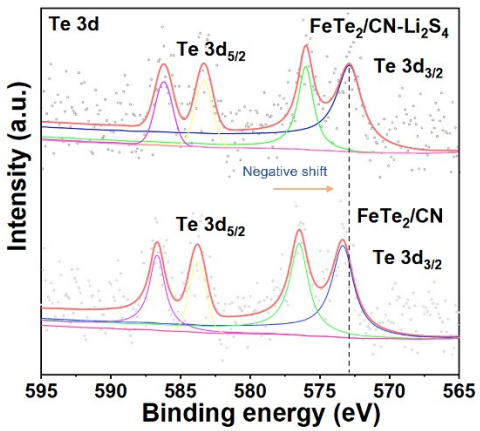

Fig. S11 High-resolution Te 3d XPS spectra of $FeTe_2$/CN before and after Li_2S_4 adsorption.

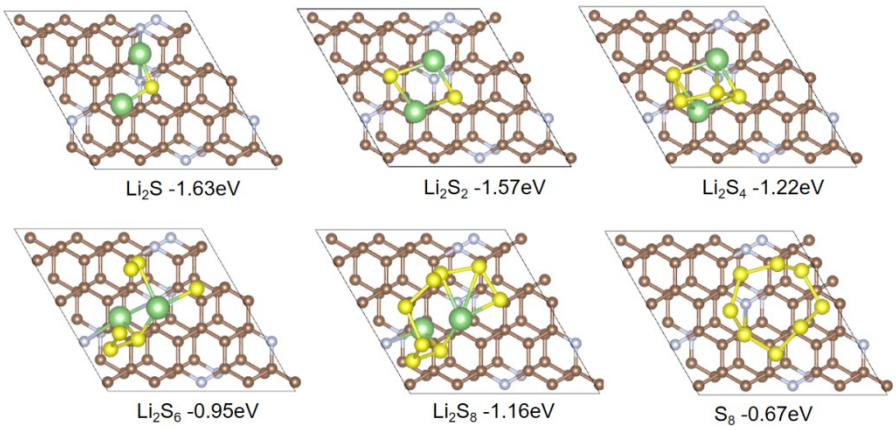

Fig. S12 DFT calculation results of optimized geometrical configurations of the surface of CN with LiPS (Li_2S, Li_2S_2, Li_2S_4, Li_2S_6, Li_2S_8, and S_8).

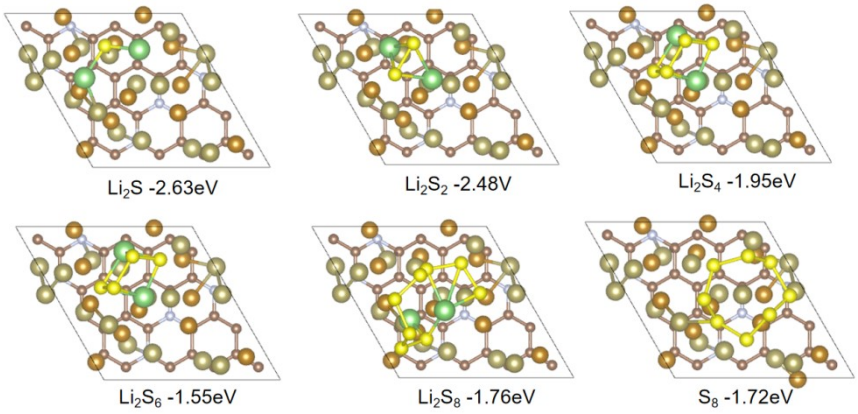

Fig. S13 DFT calculation results of optimized geometrical configurations of the surface of $FeTe_2$/CN with LiPS (Li_2S, Li_2S_2, Li_2S_4, Li_2S_6, Li_2S_8, and S_8)

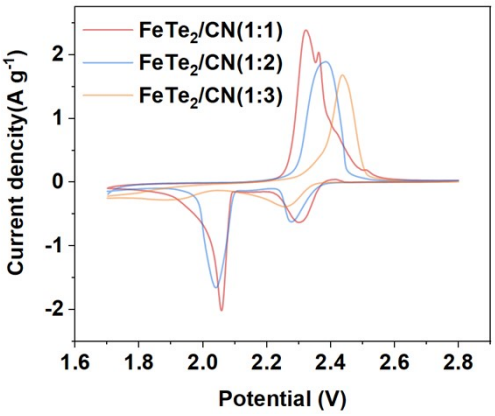

Fig. S14 CV tests of the S@$FeTe_2$/CN electrode with different mass ratio of the ZIF-8 and $Fe(C_5H_7O_2)_3$.

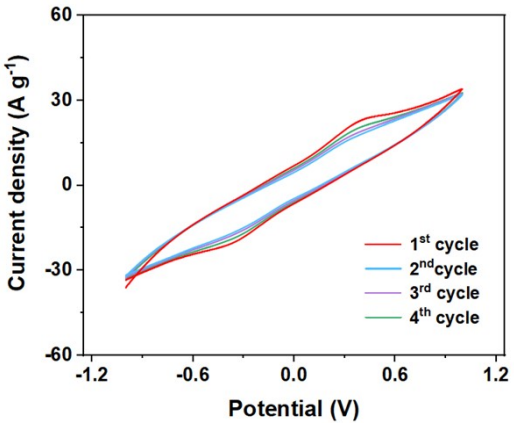

Fig. S15 CV curves of symmetric cells of $FeTe_2$/CN worked as electrodes at a scan rate of 20 mV s^{-1} for the first four cycles.

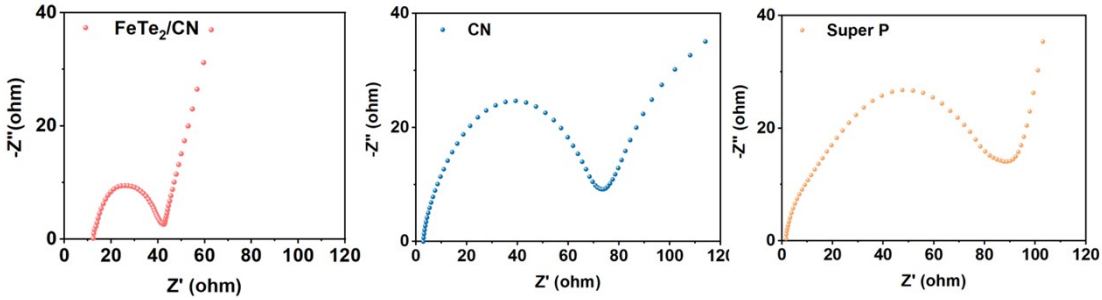

Fig. S16 EIS spectrum of S@$FeTe_2$/CN, S@CN, and S@Super/S electrodes before cycling.

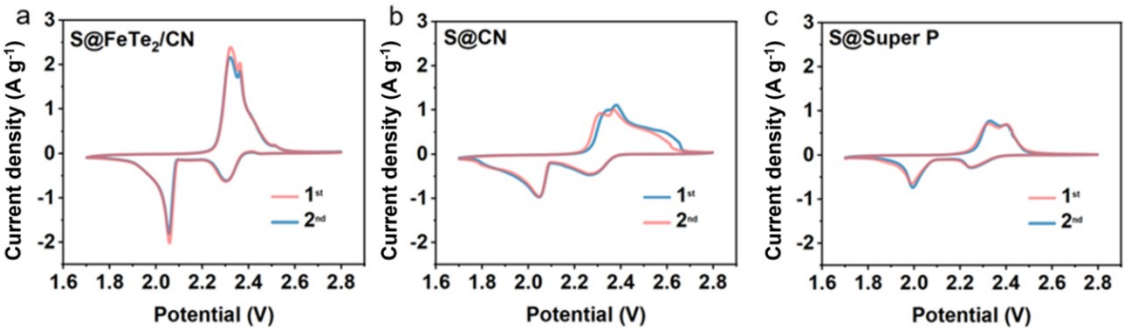

Fig. S17 First two cycles of CV curves of a) S@$FeTe_2$/CN, b) S@CN, and c) S@Super P carried out at a scan rate of 0.1 mV s^{-1}.

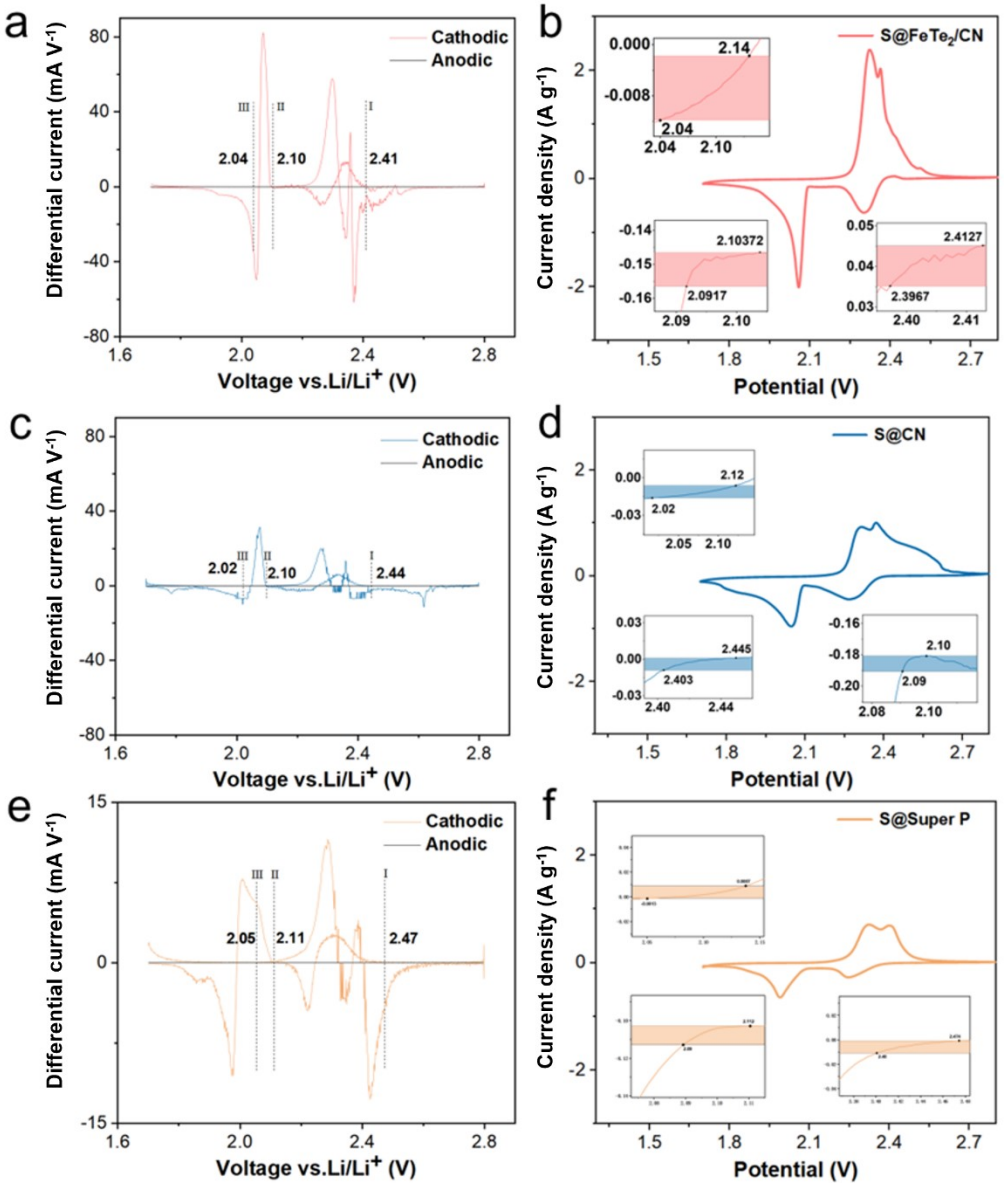

Fig. S18 Differential CV curves of a) S@$FeTe_2$/CN, c) S@CN and e) S@Super P. The base line voltage and current density are defined as the value before the redox peak, where the variation on current density is the smallest, named as dI/dV = 0. The value of the base line voltages for cathodic peak I, II and anodic peak III were calculated, respectively. CV curves and corresponding onset potentials of redox peak I, II, and III (inset): b) S@$FeTe_2$/CN, d) S@CN and f) S@Super P. Following a common definition employed in electrocatalysis, the onset potential is determined when the current density is 10 μA cm^{-2} beyond the corresponding baseline current density (more specifically, 10 μA cm^{-2} more negative than baseline current density for cathodic peaks or 10 μA cm^{-2} positive than baseline current density for anodic peaks). As shown in the inset of b, d, and f, the baseline voltages are the same as in a, c, and e while the colored region indicates the gap in current density.

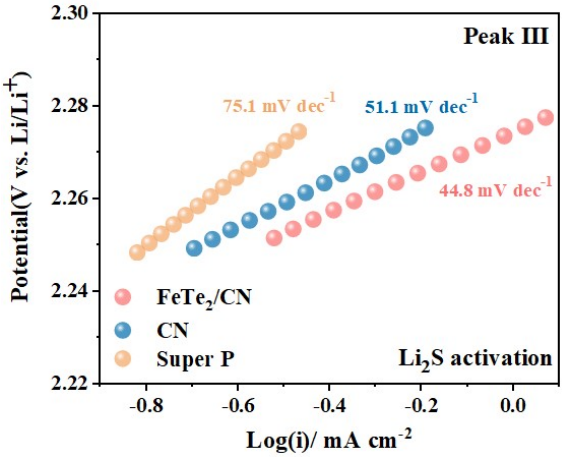

Fig. S19 Tafel plots of coin cell using $FeTe_2$/CN, CN and Super P as electrodes of the CV curves, respectively (Peak III).

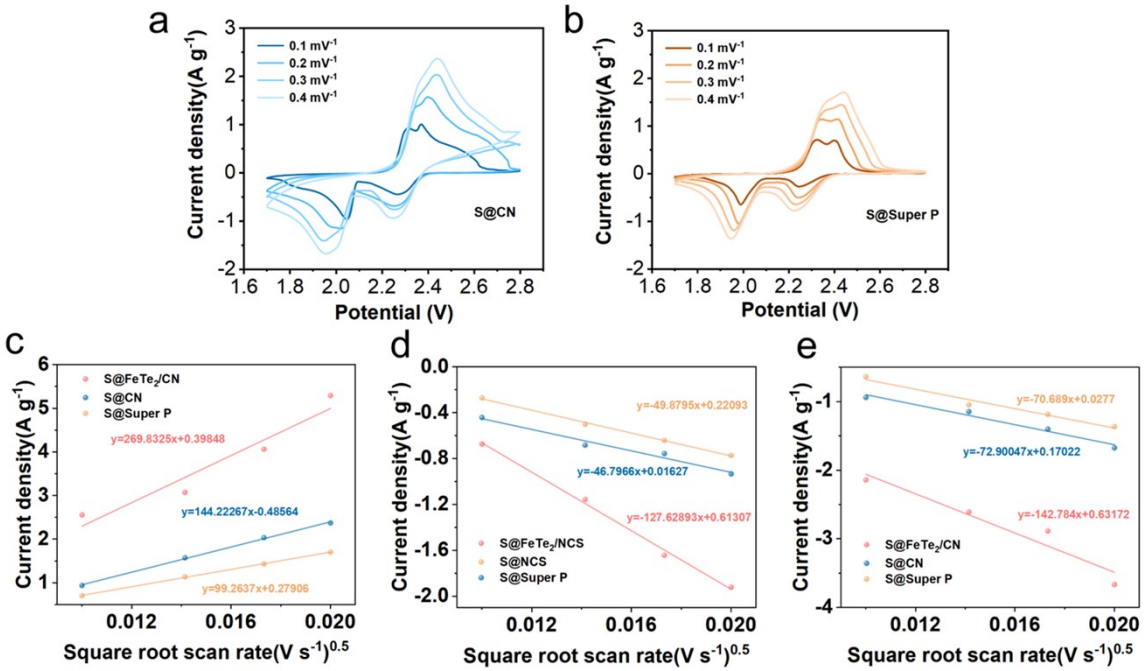

Fig. S20 a) CV curves of S@CN and b) S@Super P at different scan rates. c) Plots of CV peak current for the first cathodic reduction, d) the second cathodic reduction, e) anodic oxidation process *vs* the square root of the scan rates.

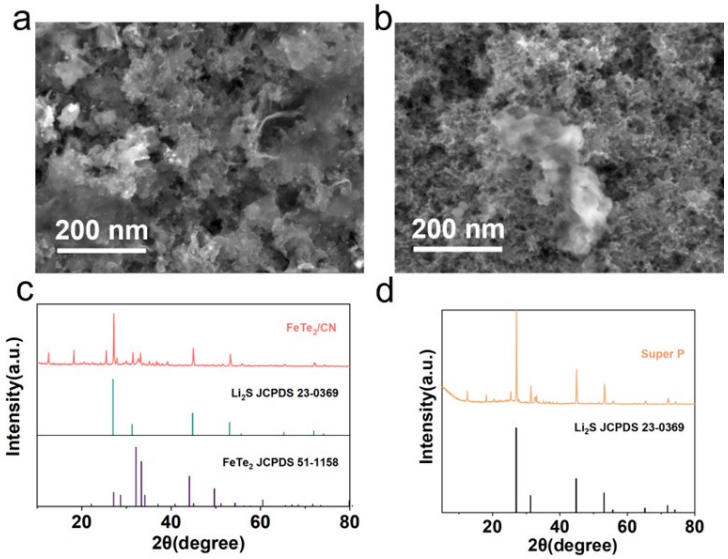

Fig. S21 SEM images and XRD patterns of electrodes after Li2S nucleation. a, c) $FeTe_2$/CN, b, d) Super P.

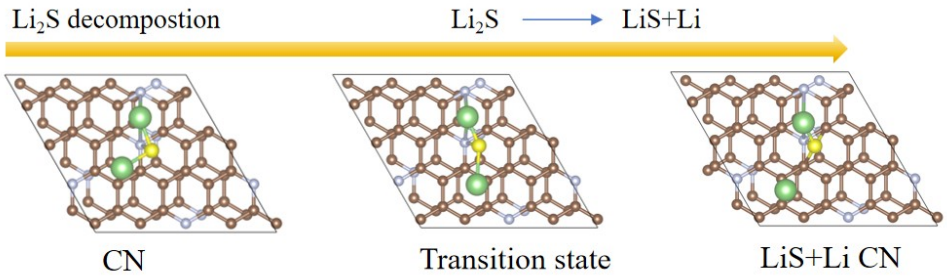

Fig. S22 The optimized adsorption configuration of Li_2S decomposition on CN.

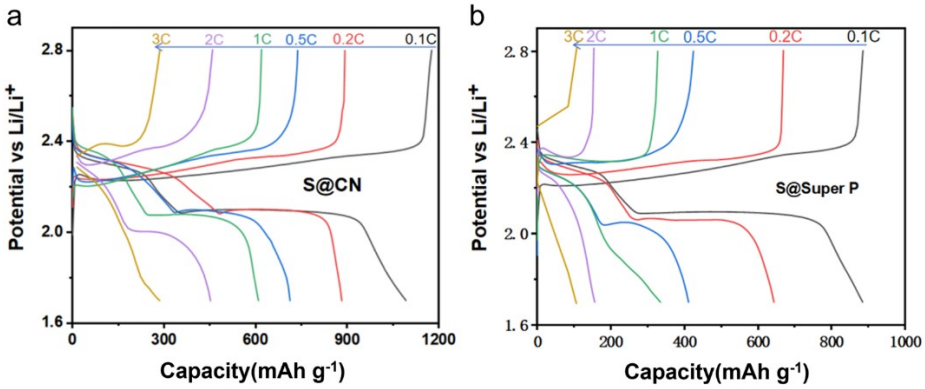

Fig. S23 Galvanostatic charge−discharge profiles of a) S@CN and b) S@Super P at different current densities range from 0.1 C to 3 C.

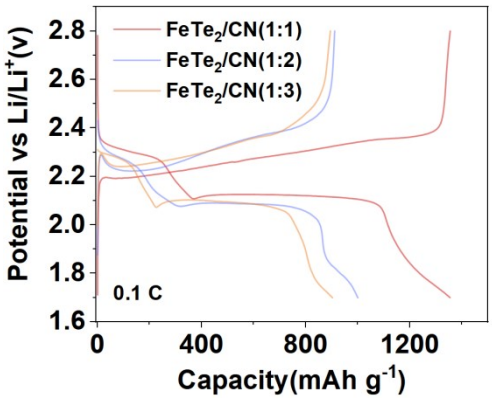

Fig. S24 Galvanostatic charge-discharge profiles of the S@$FeTe_2$/CN electrode with different mass ratio of the ZIF-8 and $Fe(C_5H_7O_2)_3$.

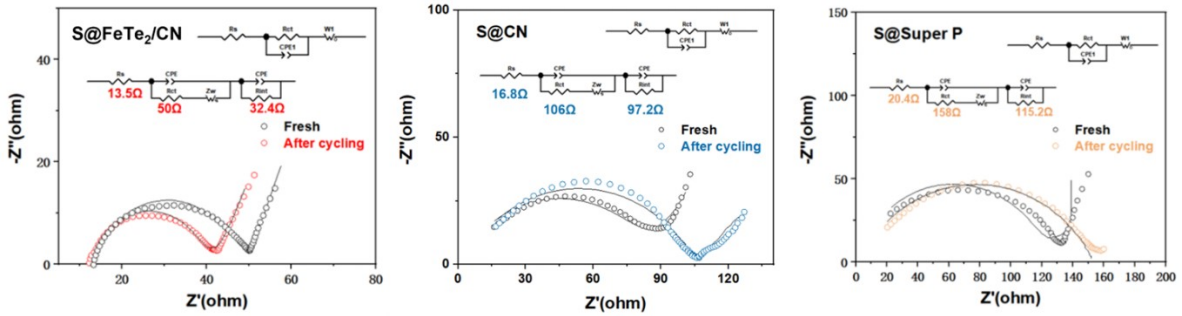

Fig. S25 EIS spectrum of S@$FeTe_2$/CN, S@CN and S@Super P before and after cycling at 1 C for 200 cycles.

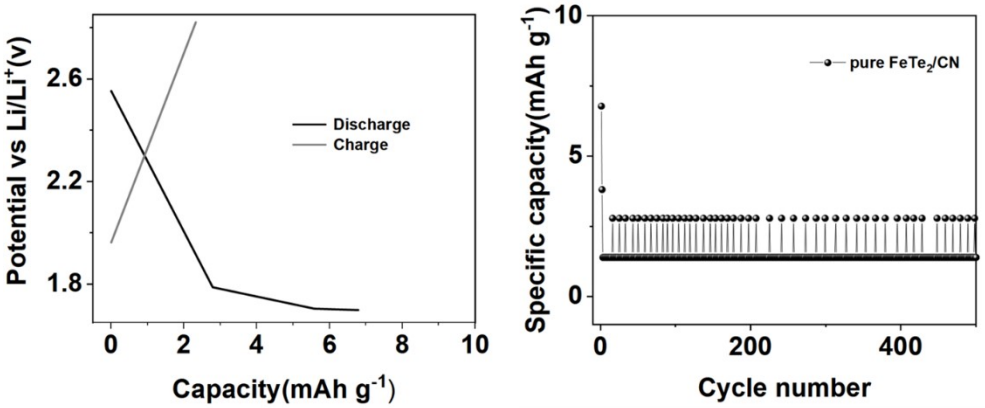

Fig. S26 Charge/discharge curves and cycling stability of pure $FeTe_2$/CN measured in the same electrochemical conditions.

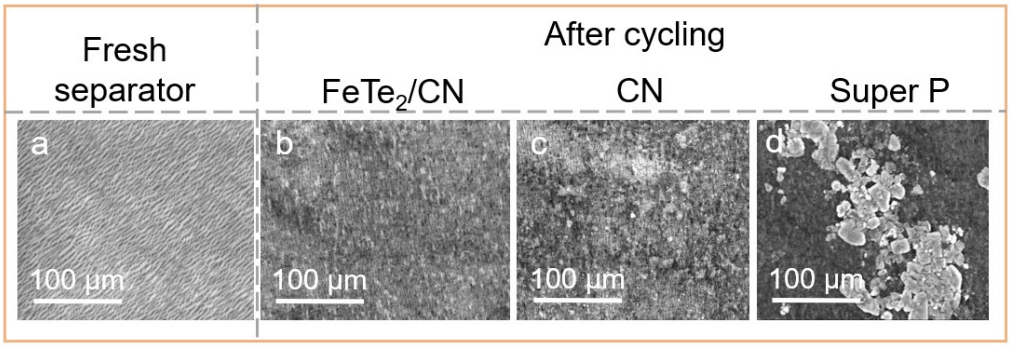

Fig. S27 SEM images of a) pristine Celgard 2400 separator and b-d) the separators obtained from disassembling cycled coin cells based on $FeTe_2$/CN, CN, and Super P as the S host.

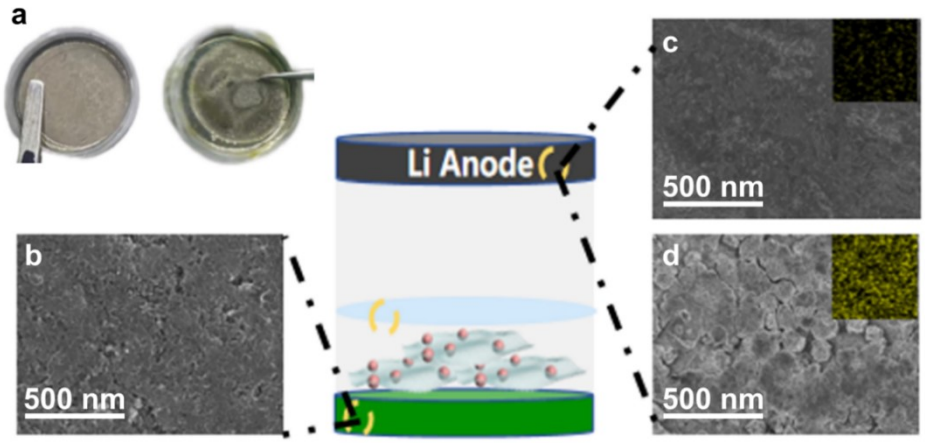

Fig. S28 SEM images of a) pristine Celgard 2400 separator and b-d) the separators obtained from disassembling cycled coin cells based on $FeTe_2$/CN, CN, and Super P as the S host.

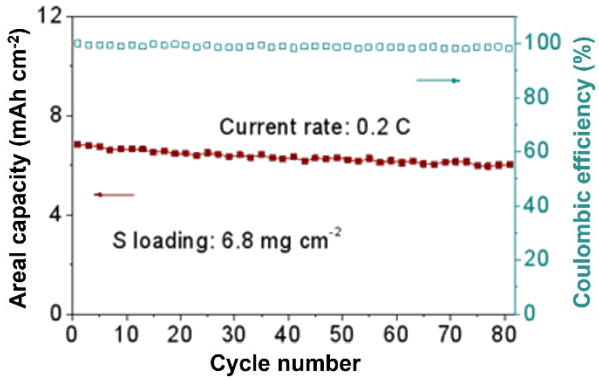

Fig. S29 Galvanostatic charge/discharge profiles of S@$FeTe_2$/CN at various current rates with a high sulfur loading of 6.8 mg cm^{-2} at 0.2 C.

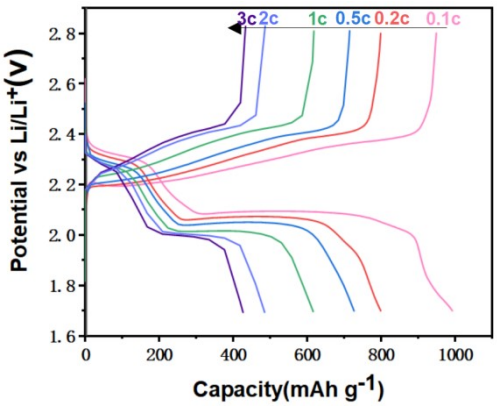

Fig. S30 Galvanostatic charge/discharge profiles of S@$FeTe_2$/CN at various current rates with a high sulfur loading of 3.3 mg cm^{-2} at 0.1 C, 0.2 C, 0.5 C, 1 C, 2 C, 3 C.

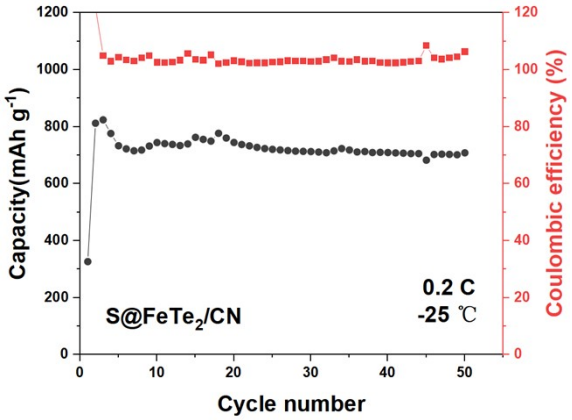

Fig. S31 Cycling performance of the S@$FeTe_2$/CN electrode at 0.2 C under a temperature of −25 °C.

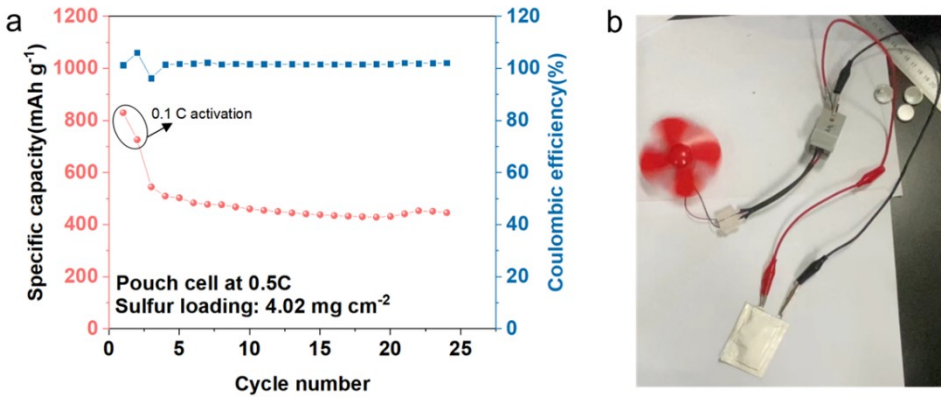

Fig. S32 a) Cyclic performance of the assembled S@$FeTe_2$/CN-based pouch cells at 0.5 C. b) Optical picture of electric fan powered by S@$FeTe_2$/CN-based pouch cells.

Table S1 Comparison of the conventional synthesis condition and our 2D carbon nanosheets synthesis condition.

Precursor	Other Conditions	Temperature	Reference
MOF-74	KOH Solution	1000 °C	5
CPPhen	Highly toxic organic (chloroform solution)	850 °C	6
Polymers/ organic–inorganic blends	Highly toxic organic (tetrahydrofuran); NaOH etching	800 °C	7
Rhodanine	The assistance of modifier (sodium chloride)	1000 °C	8
ZIF-8	**/**	**620 °C**	**This work**

Table S2 Summary of the comparison of $FeTe_2$/CN electrochemical performance as host cathode for LSBs with state-of-the-art Fe-based or chalcogenide-based materials.

Host material	Capacity (mAh g^{-1}) (current rate)	(cycles, current rate)	Decay rate (per cycle, %)	Ref
FeP/rGO/CNTs	1271.6 (0.1 C)	(400, 1 C)	0.04%	9
Fe/Fe_3C-MWCNT@ACT	1273 (0.1 C)	(1000, 1 C)	0.05%	10
Fe_3O_4@C	1243 (0.1 C)	(300, 1 C)	0.14%	11
Cu_xS@NC/S-F	1432 (0.1 C)	(500, 2 C)	0.058%	12
NiS_2@NC	1150 (0.2 C)	(500, 1 C)	0.15%	13
N-CN@Co_3Se_4	1437 (0.1 C)	(800, 0.2 C)	0.067%	14
VSe_2-VG@CC	1025 (0.5 C)	(800, 5 C)	0.039%	15
Sb_2Se_3/rGO	1160 (0.2 C)	(500, 1 C)	0.057%	16
ZnTe@NC	1005 (0.1 C)	(500, 1 C)	0.15%	17
h-$CoTe_2$/NG	960.1 (0.5 C)	(200, 0.5 C)	0.139%	18
$FeTe_2$/CN	**1353.4 (0.1 C)**	**(1500, 3 C)**	**0.029%**	**This work**

References

1 G. Kresse, J. Furthmüller, *Phys.Rev.B* **1996**, *54*, 11169.

2 L. Han, F. Jing, X.-Z. Luo, Y.-L. Zhong, K. Wang, S.-H. Zang, D.-H. Teng, Y. Liu, J. Chen, C. Yang, *Appl. Catal., B* **2021**, *282*, 119602.

3 X. Zhao, J. Chen, Z. Bi, S. Chen, L. Feng, X. Zhou, H. Zhang, Y. Zhou, T. Wågberg, G. Hu, *Adv. Sci.* **2023**, *10*, 2205889.

4 O. Hurtado-Aular, R. Anez, A. Sierraalta, *Surf. Sci.* **2021**, *714*, 121907.

5 P. Pachfule, D. Shinde, M. Majumder, Q. Xu, *Nat. Chem.* **2016**, *8*, 718-724.

6 T. Mori, H. Tanaka, A. Dalui, N. Mitoma, K. Suzuki, M. Matsumoto, N. Aggarwal, A. Patnaik, S. Acharya, L. K. Shrestha, *Angew. Chem. Int. Ed.* **2018**, *57*, 9679-9683.

7 S. Kim, M. Ju, J. Lee, J. Hwang, J. Lee, *J. Am. Chem. Soc.* **2020**, *142*, 9250-9257.

8 Y. Chen, B. Xi, M. Huang, L. Shi, S. Huang, N. Guo, D. Li, Z. Ju, S. Xiong, *Adv. Mater.* **2022**, *34*, 2108621.

9 S. Huang, Y. Von Lim, X. Zhang, Y. Wang, Y. Zheng, D. Kong, M. Ding, S. A. Yang, H. Y. Yang, *Nano Energy* **2018**, *51*, 340-348.

10 R. Chen, Y. Zhou, X. Li, *Nano Lett.* **2022**, *22*, 1217-1224.

11 W. Sun, Y. Li, S. Liu, C. Liu, X. Tan, K. Xie, *Chem. Eng. J.* **2021**, *416*, 129166.

12 Q. Yu, Y. Lu, R. Luo, X. Liu, K. Huo, J. K. Kim, J. He, Y. Luo, *Adv. Funct. Mater.* **2018**, *28*, 1804520.

13 C. Huang, J. Yu, C. Y. Zhang, Z. Cui, J. Chen, W. H. Lai, Y. J. Lei, B. Nan, X. Lu, R. He, *Adv. Mater.* **2024**, 2400810.

14 D. Cai, B. Liu, D. Zhu, D. Chen, M. Lu, J. Cao, Y. Wang, W. Huang, Y. Shao, H. Tu, *Adv. Energy Mater.* **2020**, *10*, 1904273.

15 H. Ci, J. Cai, H. Ma, Z. Shi, G. Cui, M. Wang, J. Jin, N. Wei, C. Lu, W. Zhao, *ACS Nano* **2020**, *14*, 11929-11938.

16 Y. Tian, G. Li, Y. Zhang, D. Luo, X. Wang, Y. Zhao, H. Liu, P. Ji, X. Du, J. Li, *Adv. Mater.* **2020**, *32*, 1904876.

17 C. Huang, J. Yu, C. Li, Z. Cui, C. Zhang, C. Zhang, B. Nan, J. Li, J. Arbiol, A. Cabot, *Adv. Funct. Mater.* **2023**, *33*, 2305624.

18 B. Li, P. Wang, J. Yuan, N. Song, J. Feng, S. Xiong, B. Xi, *Adv. Mater.* **2024**, *36*, 2309324.